0254-6124/2012/32(3)-305–07 *Chin. J. Space Sci.* 空间科学学报

Huang Zhaohui, Ding Kai, Wang Chi. Effect of the interplanetary electric field on the magnetopause from global MHD simulations. *Chin. J. Space Sci.*, 2012, **32**(2): 305-311

Effect of the Interplanetary Electric Field on the Magnetopause From Global MHD Simulations*

HUANG Zhaohui[1] DING Kai[1,2] WANG Chi[1]

1(*State Key Laboratory of Space Weather, Center for Space Science and Applied Research, Chinese Academy of Sciences, Beijing* 100190)

2(*Graduate University of Chinese Academy of Sciences, Beijing* 100094)

Abstract The north-south component B_z of the Interplanetary Magnetic Field (IMF) and solar wind dynamic pressure $P_{\rm d}$ are generally treated as the two main factors in the solar wind that determine the geometry of the magnetosphere. By using the 3D global MHD simulations, we investigate the effect of the Interplanetary Electric Field (IEF) on the size and shape of magnetopause quantitatively. Our numerical experiments confirm that the geometry of the magnetopause are mainly determined by $P_{\rm d}$ and B_z, as expected. However, the dawn-dusk IEFs have great impact on the magnetopause erosion because of the magnetic reconnection, thus affecting the size and shape of the magnetopause. Higher solar wind speed with the same B_z will lead to bigger dawn-dusk IEFs, which means the higher reconnection rate, and then results in more magnetic flux removal from the dayside. Consequently, the dayside magnetopause moves inward and flank magnetopause moves outward.

Key words Dynamic pressure, Interplanetary Electric Field (IEF), Magnetopause

Classified index P 353

0 Introduction

Magnetopause is the magnetic boundary between the solar wind and the Earth's field, which separates the magnetospheric plasma from the solar wind and determines the size of the magnetosphere. The models for location and shape of the magnetopause are very important for space weather forecast. The location and shape of the magnetopause have been studied by many researchers for more than four decades. Chapman and Ferraro[1] first introduced the concept of the magnetopause boundary which depends on the balance of the solar wind dynamic pressure $P_{\rm d}$ and magnetic pressure of the magnetosphere. Ferraro[2] first calculated the shape of the magnetopause. Aubry *et al.*[3] and Fairfield[4] recognized that the orientation of interplanetary magnetic IMF also affects the magnetopause locations. Many models of the magnetopause location[4−16] were developed, in which the $P_{\rm d}$ and B_z had been seen as two main factors. But dynamic pressure $P_{\rm d}$ is a composite result of solar wind number density and speed. In the previous work about energy conversion on the magnetopause, such as Ref.[17], speed has a much stronger effect on the

* Supported by the National Natural Science Foundation of China (40674082, 40974106, 40921063, 40831060) and the Specialized Research Fund for State Key Laboratories

Received January 23, 2011. Revised November 22, 2011

E-mail: zhhuang@spaceweather.ac.cn

total reconnection efficiency.

In this study, using the 3D global MHD simulations, first, through comparing the different numerical results with the same $P_{\rm d}$ and B_z under various combinations of solar wind density and speed, we find the different combinations of density and speed have different effects on the magnetopause location under the constant $P_{\rm d}$; second, by analyzing the numerical results when $P_{\rm d}$ increases from 1.336 nPa to 5.336 nPa by varying density from 5 $\rm cm^{-3}$ to 20 $\rm cm^{-3}$ and speed from 400 $\rm km{\cdot}s^{-1}$ to 800 $\rm km{\cdot}s^{-1}$ respectively, we propose the geometry of magnetopause is affected by v_xB_z, which is also the magnitude of the IEFs besides the $P_{\rm d}$ and B_z.

1 Model

In this study, we use a global magnetospheric MHD simulation code[18−19], on the basis of an extension of the Lagrangian version of the piecewise parabolic method (PPMLR)[20]. The PPMLR-MHD algorithm has a formal accuracy of the third order in space and the second order in time, and a low numerical dissipation. This PPMLR-MHD code has been extended to its parallel version and used to study the interaction of the Interplanetary (IP) shocks with the magnetosphere and the effect of IP shock strengths and orientations on Storm Sudden Commencement (SSC) rise times[21−24]. The model can simulate the global behavior of the solar wind-magnetosphere-ionosphere system.

We solve the ideal MHD equations as follows.

$$\frac{\partial}{\partial t}\begin{bmatrix}\rho\\ \rho\boldsymbol{v}\\ \boldsymbol{B}\\ E\end{bmatrix}+\nabla\begin{bmatrix}\rho\boldsymbol{v}\\ \rho\boldsymbol{v}\boldsymbol{v}+I\left(p+\dfrac{1}{2\mu}B^2\right)-\dfrac{1}{\mu}\boldsymbol{B}\boldsymbol{B}\\ \boldsymbol{v}\boldsymbol{B}-\boldsymbol{B}\boldsymbol{v}\\ \left(E+p+\dfrac{1}{2\mu}B^2\right)\boldsymbol{v}-\dfrac{1}{\mu}(\boldsymbol{v}\cdot\boldsymbol{B})\boldsymbol{B}\end{bmatrix}=\begin{bmatrix}0\\ \rho\boldsymbol{g}\\ 0\\ \rho\boldsymbol{v}\cdot\boldsymbol{g}\end{bmatrix}.$$

Here ρ is the plasma density, p is the pressure, and $\boldsymbol{v}$ is the speed.

$$E=\frac{\rho}{\gamma-1}+\frac{1}{2}\rho v^2+\frac{1}{2\mu}B^2$$

is the total energy density of plasma. $\boldsymbol{I}$ and $\boldsymbol{g}$ are the unity matrix and the acceleration due to gravity, respectively. We take $\gamma=5/3$ for the ratio of specific heats. Since reconnection is mathematically forbidden in ideal MHD and only allowed by the presence of some kinds of diffusion, the nature and amount of diffusion in a simulation code are crucial to what kind of reconnection it produces. Numerical diffusion inherent in PPMLR algorithm used in global MHD simulations mimics the effects of physical resistivity, diffusion, and viscosity. The role of numerical diffusion is rather positive in global MHD simulations of the SW-M-I system and the parallel electric field created by numerical diffusion is thus physically meaningful. PPMLR algorithm has numerical diffusion that is confined in the reconnection region and is negligible otherwise.

The MHD equations represent coupling of the fluid dynamic equations with the Maxwell's equations of electrodynamics, and describe the conservation of mass, momentum, magnetic flux, and energy. The numerical box is taken to be $-300\,R_{\rm e}\leqslant x\leqslant 30\,R_{\rm e}$, $-150\,R_{\rm e}\leqslant y,\ z\leqslant 150\,R_{\rm e}$, and it is divided into $160\times160\times160$ grid points. The finite difference method with Piecewise Parabolic Method (PPM) and Riemann solver were chosen for computation scheme; this scheme has a formal accuracy of the third order in space and the second order in time and a low numerical dissipation. PPM has three steps:

(1) In Lagrangian coordinates, we implement the piecewise parabolic interpolations, compute the effective left and right states and solve the Riemann problems at each zone interface in order to determine the new zone averages on the Lagrangian grids;

(2) Calculate the updated zone averages by differencing the Lagrangian fluxes, get new piecewise parabolic interpolations and integrate those of each variable over regions of overlap between the Lagrangian and Eulerian grids;

(3) Map quantities from the Lagrangian grid back to the Eulerian grid, and difference then to obtain the final zone averages on the Eulerian grid.

All numerical examples are made by Global MHD simulations under the following simplifying assumptions: (a) solar wind is along the Sun-Earth line, (b) IMF is north-south, (c) ionosphere is assumed uniform with non-zero Pedersen conductance only, and (d) simulation solution is in a quasi-steady state. Each solution is characterized by three adjustable parameters, the solar wind number density $N_{\rm sw}$, the solar wind speed $v_{\rm sw}$, southward IMF B_z, all other solar wind parameters are fixed, including the Pedersen conductance $\Sigma_{\rm p} = 5\,{\rm S}$ and temperature $T = 0.91 \times 10^5\,{\rm K}$.

2 Simulation Results

Dynamic pressure $P_{\rm d} = \rho v^2$ is the composite result of solar wind density $N_{\rm sw}$ and speed $v_{\rm sw}$. We have run two types of cases. One is run with various combinations of solar wind density and speed under constant $P_{\rm d} = 2\,{\rm nPa}$ when B_z equals 5, −5, −10, −20 nT respectively (Table 1∼4, the other is run with $P_{\rm d}$ increasing from 1.336 nPa to 5.336 nPa by varying solar wind density from $5\,{\rm cm^{-3}}$ to $20\,{\rm cm^{-3}}$ and speed from $400\,{\rm km{\cdot}s^{-1}}$ to $800\,{\rm km{\cdot}s^{-1}}$ respectively (Table 5∼10). In this paper, we use $x_{\rm mp}$, $y_{\rm mp}$, $z_{\rm mp}$, the intersections of the magnetopause with GSM coordinate axes, to stand for the magnetopause location. $x_{\rm mp}$, $y_{\rm mp}$, $z_{\rm mp}$ are the subsolar point, the flank point, and the top point of magnetopause. There are four methods pressure and density maxima, current density maximum, and the streamline method to search the magnetopause location, but no obvious differences among them[25]. In this section, the points are searched from the maximum of current density.

2.1 Computational Results of Different Solar Wind Density and Speed With $P_{\rm d}$ =2 nPa

There are four runs with $B_z = 5$, −5, −10, −20 nT, $P_{\rm d} = 2\,{\rm nPa}$, respectively. In each run we have stepwise changed solar wind density and speed when dynamic pressure remains unchanged. The numerical results of four runs are presented in Tables 1∼4 ($x_{\rm mp}^{\rm error}$, $y_{\rm mp}^{\rm error}$, $z_{\rm mp}^{\rm error}$ are the biggest grid distances in the magnetopause location and the signs of significant changes of $x_{\rm mp}$, $y_{\rm mp}$, $z_{\rm mp}$).

Table 1 Geometrical parameters of magnetopause versus different combinations of $N_{\rm sw}$, $v_{\rm sw}$ with $P_{\rm d} = 2\,{\rm nPa}$ for $B_z = 5\,{\rm nT}$ ($x_{\rm mp}^{\rm error} = 0.4\,R_{\rm e}$, $y_{\rm mp}^{\rm error} = 0.58\,R_{\rm e}$, $z_{\rm mp}^{\rm error} = 0.61\,R_{\rm e}$)

$N_{\rm sw}/{\rm cm^{-3}}$	$v_{\rm sw}/({\rm km{\cdot}s^{-1}})$	$x_{\rm mp}/R_{\rm e}$	$y_{\rm mp}/R_{\rm e}$	$z_{\rm mp}/R_{\rm e}$
2	774	9	13.2	13.5
3	632	9.8	13.2	13.5
4	547	9.8	13.2	13.5
5	489	9.8	13.0	13.5
6	447	9.8	13.0	13.4
7	414	9.8	13.0	13.4
8	387	9.8	13.0	13.4
9	365	9.8	13.0	13.4
10	346	9.8	13.0	13.4
15	283	9.8	12.6	13.4
20	245	9.8	12.6	13.3

Table 2 Geometrical parameters of magnetopause versus different combinations of $N_{\rm sw}$, $v_{\rm sw}$ with $P_{\rm d} = 2\,{\rm nPa}$ for $B_z = -5\,{\rm nT}$ ($x_{\rm mp}^{\rm error} = 0.4\,R_{\rm e}$, $y_{\rm mp}^{\rm error} = 0.48\,R_{\rm e}$, $z_{\rm mp}^{\rm error} = 0.76\,R_{\rm e}$)

$N_{\rm sw}/{\rm cm^{-3}}$	$v_{\rm sw}/({\rm km{\cdot}s^{-1}})$	$x_{\rm mp}/R_{\rm e}$	$y_{\rm mp}/R_{\rm e}$	$z_{\rm mp}/R_{\rm e}$
2	774	8.2	12.0	16.4
3	632	8.6	12.0	16.1
4	547	8.6	12.0	15.9
5	489	8.6	12.0	15.8
6	447	8.6	12.0	15.6
7	414	8.6	11.6	15.4
8	387	8.6	11.6	15.2
9	365	8.6	11.6	15.2
10	346	8.6	11.4	15.2
15	283	8.6	11.4	15.2
20	245	8.6	11.0	14.6

In Table 1 ($B_z = 5\,{\rm nT}$, $P_{\rm d} = 2\,{\rm nPa}$), when solar wind density increases (speed decreases), the $x_{\rm mp}$ has no change, the $y_{\rm mp}$ decreases from $13.2\,R_{\rm e}$ to $12.6\,R_{\rm e}$,

the $z_{\rm mp}$ decreases from 13.5 $R_{\rm e}$ to 13.3 $R_{\rm e}$. Compared with $x_{\rm mp}^{\rm error}$, $y_{\rm mp}^{\rm error}$, $z_{\rm mp}^{\rm error}$, it is reasonable to ignore the shift distance of magnetopause location, so the different combinations of $N_{\rm sw}$, $v_{\rm sw}$ in the condition of (B_z = 5 nT, $P_{\rm d}$ = 2 nPa) have no effect on the numerical results. In Table 2, there are big differences with various combinations of $N_{\rm sw}$, $v_{\rm sw}$. With increasing density (decreasing speed), the subsolar point $x_{\rm mp}$ moves sunward, the flank point $y_{\rm mp}$ and the top point $z_{\rm mp}$ decrease. It is obvious that the magnetopause location has very different results with the various combinations of solar wind density and speed. Similar results are showed in Table 3 and Table 4. It implies that in the global MHD simulation solar wind density and speed play different roles on the magnetopause location. Compared with the results in Table 1 (B_z = 5 nT, $P_{\rm d}$ = 2 nPa), it is noted that the magnetopause location has changed much under southward IMF. The comparison in Table 1 ~4 has already suggested that when $P_{\rm d}$ = 2 nPa is constant, different combinations of solar wind density and speed impact on the magnetopause location only when IMF is southward, but have very little effect when IMF is northward. In the next section we vary the solar wind density and speed separately to study the effects of these two variables.

Table 3 Geometrical parameters of magnetopause versus different combinations of $N_{\rm sw}$, $v_{\rm sw}$ with $P_{\rm d}$ = 2 nPa for B_z = −10 nT ($x_{\rm mp}^{\rm error}$ = 0.4 $R_{\rm e}$, $y_{\rm mp}^{\rm error}$ = 0.55 $R_{\rm e}$, $z_{\rm mp}^{\rm error}$ = 0.72 $R_{\rm e}$)

$N_{\rm sw}$/cm^{-3}	$v_{\rm sw}$/(km·s^{-1})	$x_{\rm mp}/R_{\rm e}$	$y_{\rm mp}/R_{\rm e}$	$z_{\rm mp}/R_{\rm e}$
1.2	1000	7.4	13.0	15.8
1.48	900	7.4	13.0	16.1
1.87	800	7.4	13.0	16.0
2	774	7.4	13.0	16.0
3	632	7.8	12.4	15.6
4	547	7.8	12.0	15.2
5	489	7.8	11.4	14.9
6	447	7.8	11.6	15.0
7	414	7.8	11.6	15.1
8	387	8.2	11.6	15.0
9	365	8.2	11.6	15.0
10	346	8.2	11.4	15.0
15	283	8.2	11.4	14.8

Table 4 Geometrical parameters of magnetopause versus different combinations of $N_{\rm sw}$, $v_{\rm sw}$ with $P_{\rm d}$ = 2 nPa for B_z = −20 nT ($x_{\rm mp}^{\rm error}$ = 0.4 $R_{\rm e}$, $y_{\rm mp}^{\rm error}$ = 0.5 $R_{\rm e}$, $z_{\rm mp}^{\rm error}$ = 0.72 $R_{\rm e}$)

$N_{\rm sw}$/cm^{-3}	$v_{\rm sw}$/(km·s^{-1})	$x_{\rm mp}/R_{\rm e}$	$y_{\rm mp}/R_{\rm e}$	$z_{\rm mp}/R_{\rm e}$
1.2	1000	6.6	13.0	16.4
1.48	900	7.0	12.6	16.0
1.87	800	7.0	12.4	16.0
2	774	7.0	12.4	16.0
3	632	7.0	12.4	15.5
4	547	7.0	12.4	15.5
5	489	7.0	12.4	15.2
6	447	7.4	12.4	15.2
7	414	7.4	12.4	15.1
8	387	7.4	12.4	14.4
9	365	7.4	12.0	14.4
10	346	7.4	12.0	14.5
15	283	7.4	12.0	14.2

2.2 Effects of Solar Wind Density and Speed on Magnetopause Location

In the last section, different combinations of $N_{\rm sw}$, $v_{\rm sw}$ have different numerical results when IMF is southward. In this section, we examine the roles of solar density and speed separately. There are six runs (B_z = −5, −10, −20 nT, respectively), when $v_{\rm sw}$ varies from 400 km·s^{-1} to 800 km·s^{-1}, $N_{\rm sw}$ varies from 5 cm^{-3} to 20 cm^{-3} during a change of $P_{\rm d}$ from 1.336 nPa to 5.336 nPa separately. The results are in Table 5∼10. In the Table 5∼10, when $P_{\rm d}$ increases from 1.336 nPa to 5.336 nPa, $x_{\rm mp}$, $y_{\rm mp}$ and $z_{\rm mp}$ decrease and the magnetopause moves earthward. $\Delta x_{\rm mp}$, $\Delta y_{\rm mp}$ and $\Delta z_{\rm mp}$, the shift distance of the subsolar point, the flank point, the top point during a change of $P_{\rm d}$ from 1.336 nPa to 5.336 nPa, are showed in Figure 1.

Under the southward IMF, $\Delta x_{\rm mp}$ with increa-

Table 5 Geometrical parameters of magnetopause versus v_{sw} for $B_z = -5$ nT, $N_{sw} = 5$ cm^{-3}

v_{sw}/(km·s^{-1})	P_d/nPa	x_{mp}/R_e	y_{mp}/R_e	z_{mp}/R_e	y_{mp}/x_{mp}	z_{mp}/x_{mp}
400	1.336	9.4	13	18.6	1.382 98	1.978 72
600	3.006	8.2	10.8	16.4	1.317 07	2
800	5.336	7.4	10.05	14.95	1.358 11	2.020 27

Table 6 Geometrical parameters of magnetopause versus N_{sw} for $B_z = -5$ nT, $v_{sw} = 400$ km·s^{-1}

N_{sw}/cm^{-3}	P_d/nPa	x_{mp}/R_e	y_{mp}/R_e	z_{mp}/R_e	y_{mp}/x_{mp}	z_{mp}/x_{mp}
5	1.336	9.4	13.2	18.6	1.404 26	1.978 72
10	2.672	8.2	11.5	16.2	1.402 44	1.975 61
15	4.008	8.1	11.3	13.6	1.395 06	1.679 01
20	5.334	7.8	11	12.4	1.410 26	1.589 74

Table 7 Geometrical parameters of magnetopause versus v_{sw} for $B_z = -10$ nT, $N_{sw} = 5$ cm^{-3}

v_{sw}/(km·s^{-1})	P_d/nPa	x_{mp}/R_e	y_{mp}/R_e	z_{mp}/R_e	y_{mp}/x_{mp}	z_{mp}/x_{mp}
400	1.336	8.6	13.5	16.8	1.569 77	1.953 49
600	3.006	7.4	11.5	15.8	1.554 05	2.135 14
800	5.336	7	11	15	1.571 43	2.142 86

Table 8 Geometrical parameters of magnetopause versus N_{sw} for $B_z = -10$ nT, $v_{sw} = 400$ km·s^{-1}

N_{sw}/cm^{-3}	P_d/nPa	x_{mp}/R_e	y_{mp}/R_e	z_{mp}/R_e	y_{mp}/x_{mp}	z_{mp}/x_{mp}
5	1.336	8.6	13.5	16.8	1.569 77	1.953 49
10	2.672	7.8	12.2	14.8	1.564 1	1.897 44
15	4.008	7.7	11.2	13.6	1.454 55	1.766 23
20	5.334	7.6	10.4	13	1.368 42	1.710 53

Table 9 Geometrical parameters of magnetopause versus v_{sw} for $B_z = -20$ nT, $N_{sw} = 5$ cm^{-3}

v_{sw}/(km·s^{-1})	P_d/nPa	x_{mp}/R_e	y_{mp}/R_e	z_{mp}/R_e	y_{mp}/x_{mp}	z_{mp}/x_{mp}
400	1.336	7.8	12.5	15.8	1.602 56	2.025 64
600	3.006	6.6	11.5	15	1.742 42	2.272 73
800	5.336	6.2	10.2	14.5	1.645 16	2.338 71

Table 10 Geometrical parameters of magnetopause versus N_{sw} for $B_z = -20$ nT, $v_{sw} = 400$ km·s^{-1}

N_{sw}/cm^{-3}	P_d/nPa	x_{mp}/R_e	y_{mp}/R_e	z_{mp}/R_e	y_{mp}/x_{mp}	z_{mp}/x_{mp}
5	1.336	7.8	12.5	15.8	1.602 56	2.025 64
10	2.672	7	10.6	13.8	1.514 29	1.971 43
15	4.008	6.95	10.55	13	1.517 99	1.870 5
20	5.334	6.6	10.2	12	1.545 45	1.818 18

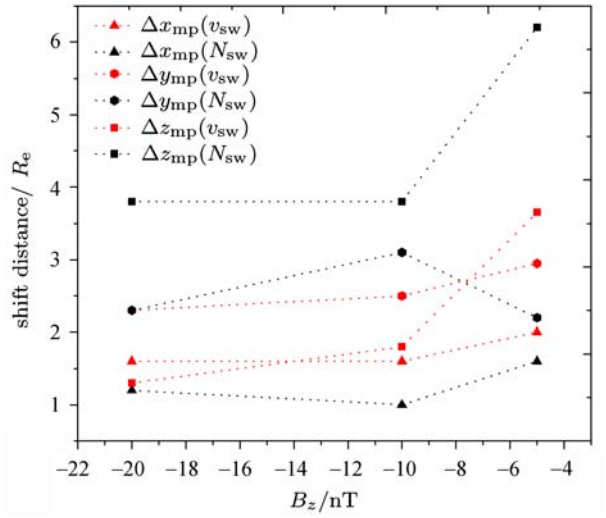

Fig. 1 Triangle, circle and square are Δx_{mp}, Δy_{mp} and Δz_{mp}, respectively (black means N_{sw}, red means v_{sw})

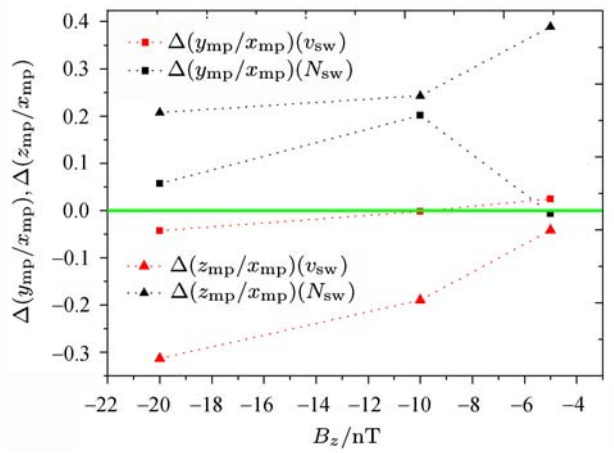

Fig. 2 Square and triangle indicate the changes of y_{mp}/x_{mp} and y_{mp}/z_{mp} respectively (black means N_{sw}, red means v_{sw})

sing solar wind speed is larger than that with increasing solar wind density. Conversely, Δy_{mp} and Δz_{mp} with increasing solar wind speed are smaller than that with increasing solar wind density. The reason maybe that the quantity $v_x B_z$, which is the rate per unit length in the equatorial plane at which the solar wind transports flux to the Earth, is also the magnitude of the solar wind Interplanetary Electric Field (IEF), according to the relation $\boldsymbol{E} = -\boldsymbol{v} \times \boldsymbol{B}$. $v_x B_z$ is the reconnection coefficient, the capability for magnetopause reconnection erosion and increases with v_{sw} when the IMF is southward. We suggest that when the southward IMF is constant, with v_{sw} changing from 400 km·s^{-1} to 800 km·s^{-1}, P_d and $v_x B_z$ increases at the same time, but only P_d increases when N_{sw} varies from 5 cm^{-3} to 20 cm^{-3}.

When v_{sw} increases from 400 km·s^{-1} to 800 km·s^{-1}, the subsolar point x_{mp} has changed more, the flank point y_{mp} and top point z_{mp} have changed smaller than that when N_{sw} increases from 5 cm^{-3} to 20 cm^{-3}. The possible reason is that due to the increasing reconnection erosion, more flux transfer from the subsolar region to the flank region, so the effect of P_d on x_{mp} is strengthened, and the effect of P_d on y_{mp} and z_{mp} is weakened. Thus, Δx_{mp} is more and Δy_{mp} and Δz_{mp} are smaller when v_{sw} changes from 400 km·s^{-1} to 800 km·s^{-1}. This can also explain the results in Table 1∼4.

Here we use $\frac{y_{mp}}{x_{mp}}$, $\frac{z_{mp}}{x_{mp}}$ to stand for the flaring of equatorial plane and meridian plane. The changes of flaring can be seen in Figure 2. The overall $\Delta(y_{mp}/x_{mp})$, $\Delta(z_{mp}/x_{mp})$ are negative (the flaring increase) with v_{sw} changing from 400 km·s^{-1} to 800 km·s^{-1}, on the contrary, $\Delta(y_{mp}/x_{mp})$, $\Delta(z_{mp}/x_{mp})$ are positive (the flaring decrease) with N_{sw} changing from 5 cm^{-3} to 20 cm^{-3}. This is consistent with our suggestion and proves it indirectly. In summary, $v_x B_z$ (IEF) need considering in constructing the new magnetopause model.

3 Discussion

In this paper, we have compared the magnetopause location with the different combinations of solar wind conditions: First, the solar wind density and speed are varied with constant P_d in Table 1∼4; Second, density and speed are varied separately in Table 5∼10. We find that the magnetopause locations are different with various composite of solar wind density and speed, which proves the solar wind density and speed have different effects on the magnetopause.

In Figure 2, we see that if only solar wind density varies from 5 cm^{-3} to 20 cm^{-3}, the flaring angle of

magnetopause decreases, while only solar wind speed varies from $400\,\mathrm{km\cdot s^{-1}}$ to $800\,\mathrm{km\cdot s^{-1}}$, the flaring angle increases. The numerical results prove that: when the B_z is southward and P_d increases only with increasing v_sw, the increasing speed makes the higher reconnection rate $v_x B_z$, which is also the magnitude of the solar wind electric field. This point is consistent with Ref.[17], so the effect of P_d on the subsolar point x_mp is strengthened because of the reconnection erosion. Consequently, more magnetic flux will transfer from subsolar region to the flank region, then the effect of P_d on y_mp, z_mp is weakened.

The conclusion suggests that the IEFs need considering to construct new magnetopause model. And the quantitative relation between the magnetopause location and IEFs will be done in further work.

References

[1] Chapman S, Ferraro V C A. A new theory of magnetic storm, I. The initial phase [J]. *J. Geophys. Res.*, 1931 (36):77

[2] Ferraro V C A. On the theory of the first phase of a geomagnetic storm: a new illustrative calculation based on idealized (plane not cylindrical) model field distribution [J]. *J. Geophys. Res.*, 1952 (57):15

[3] Aubry M B, Russell C T, Kivelson M G. Inward motion of the magnetopause before a substorm [J]. *J. Geophys. Res.*, 1970 (75):7018

[4] Fairfield D H. Average and unusual locations of the Earth's magnetopause and bow shock [J]. *J. Geophys. Res.*, 1971 (76):6700

[5] Howe H C, Binsack J H. Explorer 33 and 35 plasma observations of magnetosheath flow [J]. *J. Geophys. Res.*, 1972 (77):3334

[6] Holzer R E, Salvin J A. Magnetic flux transfer associated with expansions and contractions of the dayside magnetosphere [J]. *J. Geophys. Res.*, 1978 (83):3831

[7] Formisano V, Domingo V, Wenzel K P. The three-dimensional shape of the magnetopause [J]. *Planet. Space Sci.*, 1979 (27):1137

[8] Petrinec S M, Song P, Russell C T. Solar cycle variations in the size and shape of the magnetopause [J]. *J. Geophys. Res.*, 1991 (96):7893

[9] Sibeck D G, Lopez R E, Roelof E C. Solar cycle control of magnetoshape, location and motion [J]. *J. Geophys. Res.*, 1991 (96):5489

[10] Petrinec S M, Russell C T. An empirical model of the size and shape of the near-earth magnetotail [J]. *Geophys. Res. Lett.*, 1993 (20):2695

[11] Roelof E C, Sibeck D G. Magnetopause shape as a bivariate function of interplanetary magnetic field B_z and solar wind dynamic pressure [J]. *J. Geophys. Res.*, 1993 (98),21 421

[12] Kuznetsov S N, Suvorova A V. Solar wind control of magnetopause shape and location. Radiat. Meas., 1996 **26**(3):413

[13] Shue J H, Chao J K, Fu H C, *et al.* A new functional form to study the solar wind control of the magnetopause size and shape [J]. *J. Geophys. Res.*, 1997 (102):9497

[14] Shue J H, Song P, Russell C T, Steinberg J T, *et al.* Magnetopause location under extreme solar wind conditions [J]. *J. Geophys. Res.*, 1998 (103):17 691

[15] Kawano H, *et al.* Magnetopause shape determinations from measured position and estimates flaring angle [J]. *J. Geophys. Res.*, 1999 (104):247

[16] Dmitriev A V, Suvorova A V. Three-dimensional artificial neural network model of the dayside magnetopause [J]. *J. Geophys. Res.*, 2000 (105), 18 909

[17] Laitinen T V, *et al.* Continuous reconnection line and pressure-dependent energy conversion on the magnetopause in a global MHD model [J]. *J. Geophys. Res.*, 2007 (112):A11201

[18] Hu Y Q, Guo X C, Li G Q, Wang C, Huang Z H. Oscillation of quasi-steady Earth's magnetosphere [J]. *Chin. Phys. Lett.*, 2005 **22**(10):2723-2726

[19] Hu Y Q, Guo X C, Wang C. On the ionospheric and reconnection potentials of the Earth: Results from global MHD simulations [J]. *J. Geophys. Res.*, 2007 (112):A07215

[20] Collela P, Woodward P R. The Piecewise Parabolic Method (PPM) for gas-dynamical simulations [J]. *J. Comput. Phys.*, 1984 (54):174

[21] Wang C *et al.* 3D global simulation of the interaction of the interplanetary shocks with the magnetosphere [J]. *AIP Conf. Proc.*, 2005, **781**:320-324

[22] Wang C, Li C X, Huang Z H, Richardson J D. Effect of interplanetary shock strengths and orientations on storm sudden commencement rise times [J]. *Geophys. Res. Lett.*, 2006, **33**, L14104, doi:10.1029/2006GL025966

[23] Wang C, Liu J B, Huang Z H, Richardson J D. Response of the magnetic field in the geosynchronous orbit to solar wind dynamic pressure pulses [J]. *J. Geophys. Res.*, 2007, (112):A12210, doi:10.1029/2007JA012664

[24] Huang Z H, Wang C, Hu Y Q, Guo X C. Parallel implementation of 3D global MHD simulations for Earth's magnetosphere [J]. *Comp. Math. Appl.*, 2008 (6):55

[25] Palmroth M T *et al.* Stormtime energy transfer in global MHD simulation [J]. *J. Geophys. Res.*, 2002, **108**(A1):1048, doi:10.1029/2002JA009446, 2003